



Operando identification of site-dependent water oxidation activity on ruthenium dioxide single-crystal surfaces

Rao, Reshma R.; Kolb, Manuel J.; Giordano, Livia; Pedersen, Anders Filsøe; Katayama, Yu; Hwang, Jonathan; Mehta, Apurva; You, Hoydoo; Lunger, Jaclyn R.; Zhou, Hua

Total number of authors:
15

Published in:
Nature Catalysis

Link to article, DOI:
[10.1038/s41929-020-0457-6](https://doi.org/10.1038/s41929-020-0457-6)

Publication date:
2020

Document Version
Peer reviewed version

[Link back to DTU Orbit](#)

Citation (APA):

Rao, R. R., Kolb, M. J., Giordano, L., Pedersen, A. F., Katayama, Y., Hwang, J., Mehta, A., You, H., Lunger, J. R., Zhou, H., Halck, N. B., Vegge, T., Chorkendorff, I., Stephens, I., & Shao-Horn, Y. (2020). Operando identification of site-dependent water oxidation activity on ruthenium dioxide single-crystal surfaces. *Nature Catalysis*, 3(6), 516-525. <https://doi.org/10.1038/s41929-020-0457-6>

General rights








Copyright and moral rights for the publications made accessible in the public portal are retained by the authors and/or other copyright owners and it is a condition of accessing publications that users recognise and abide by the legal requirements associated with these rights.

- Users may download and print one copy of any publication from the public portal for the purpose of private study or research.
- You may not further distribute the material or use it for any profit-making activity or commercial gain
- You may freely distribute the URL identifying the publication in the public portal

If you believe that this document breaches copyright please contact us providing details, and we will remove access to the work immediately and investigate your claim.



Operando identification of site-dependent water oxidation activity on ruthenium dioxide single-crystal surfaces

Reshma R. Rao^{1,9,12} , Manuel J. Kolb^{2,12}, Livia Giordano^{1,2}, Anders Filsøe Pedersen³, Yu Katayama^{2,10} , Jonathan Hwang⁴, Apurva Mehta⁵, Hoydoo You⁶, Jaclyn R. Lunger⁴, Hua Zhou⁷ , Niels Bendtsen Halck⁸, Tejs Vegge⁸ , Ib Chorkendorff³ , Ifan E. L. Stephens^{3,11}  and Yang Shao-Horn^{1,2,4} 

Understanding the nature of active sites is central to controlling (electro)catalytic activity. Here we employed surface X-ray scattering coupled with density functional theory and surface-enhanced infrared absorption spectroscopy to examine the oxygen evolution reaction on RuO₂ surfaces as a function of voltage. At 1.5 V_{RHE}, our results suggest that there is an –OO group on the coordinatively unsaturated ruthenium (Ru_{CUS}) site of the (100) surface (and similarly for (110)), but adsorbed oxygen on the Ru_{CUS} site of (101). Density functional theory results indicate that the removal of –OO from the Ru_{CUS} site, which is stabilized by a hydrogen bond to a neighbouring –OH (–OO–H), could be the rate-determining step for (100) (similarly for (110)), where its reduced binding on (100) increased activity. A further reduction in binding energy on the Ru_{CUS} site of (101) resulted in a different rate-determining step (–O + H₂O – (H⁺ + e[–]) → –OO–H) and decreased activity. Our study provides molecular details on the active sites, and the influence of their local coordination environment on activity.

Catalysing the oxygen evolution reaction (OER) is pivotal for enabling efficient production of energy carriers such as hydrogen¹ and ammonia², synthetic carbon-neutral fuels by CO₂ reduction³, and metals from metal oxides⁴. Rutile RuO₂ has been considered a benchmark OER catalyst in acidic solutions, where most other oxides are unstable^{5–7}. Although bulk rutile RuO₂ consists of a ruthenium atom octahedrally coordinated to six oxygen atoms, having each oxygen atom as threefold coordinated^{6,7}, surfaces can lead to undercoordinated metal and oxygen sites being different from those of the bulk and these can catalyse bond making and breaking as they can interact with reacting molecules to compensate for undercoordination^{8,9}. Theoretical^{10,11} and experimental^{12–18} studies on the (electro)catalytic activity of RuO₂ have been focused on the (110) surface, where terraces expose a fully coordinated bridge ruthenium (Ru_{BRI}) site and a coordinatively unsaturated site (Ru_{CUS}) with fivefold coordination (Ru_{CUS}), which are bonded to threefold-coordinated oxygens (O_{3c})⁶. The Ru_{CUS} site has been identified as the active site for gas-phase oxidation of small molecules such as CO (refs. ^{12,13}), CH₃OH (ref. ¹⁴), HCl (ref. ¹⁵), NH₃ (ref. ¹⁶) and NO (ref. ¹⁷). More recently, the Ru_{CUS} on (110) has been shown to catalyse the OER in acid¹⁸ by electron-coupled deprotonation of water. Specifically, adsorbed water is deprotonated on the Ru_{CUS} to form –OH and –O; the adsorption and dehydrogenation of a second water molecule creates an –OO species on the Ru_{CUS}

that forms a strong hydrogen bond to a neighbouring –OH group (–OO–H); and the final deprotonation of –OO–H (considered to be the rate-determining step (RDS)) leads to the evolution of oxygen¹⁸. Unfortunately, Ru_{CUS} on RuO₂(110) binds the –OO intermediate more strongly than is optimal¹⁸.

Using surface facets beyond RuO₂(110) can allow for an increase in the active site (Ru_{CUS}) density and tuning of the electronic structure of the Ru_{CUS} to enhance OER activity. Although the (100) (7 Ru_{CUS} nm^{–2}) and (101) (8 Ru_{CUS} nm^{–2}) facets have more Ru_{CUS} sites than (110) (5 Ru_{CUS} nm^{–2}), the OER activity enhancement of (100) and (101) relative to (110) is not proportional to the Ru_{CUS} densities, with OER activities of around 7 and 2.5 times greater than (110)¹⁹, respectively, at 1.50 V_{RHE}. This observation suggests that Ru_{CUS} sites might have distinctive electronic structures and deprotonation energetics of adsorbed intermediates on different RuO₂ surfaces. This hypothesis is supported by recent work showing that Ru_{CUS} sites on (110), (100) and (101) bind and interact with water differently. On the (110) surface, every second water molecule dissociates to form an –OH on Ru_{CUS}, with the proton transferred to the neighbouring oxygen on Ru_{BRI} (refs. ^{18,20,21}); on the other hand, every water molecularly adsorbs onto the Ru_{CUS} of (100)²², whereas every water dissociatively adsorbs onto the Ru_{CUS} of (101), with transfer of the proton to the neighbouring bridging oxygen²². Further support comes from the fact that surface redox peaks measured on oriented

¹Department of Mechanical Engineering, Massachusetts Institute of Technology, Cambridge, Massachusetts, USA. ²Research Laboratory of Electronics, Massachusetts Institute of Technology, Cambridge, Massachusetts, USA. ³Section for Surface Physics and Catalysis, Department of Physics, Technical University of Denmark, Kongens Lyngby, Denmark. ⁴Department of Materials Science and Engineering, Massachusetts Institute of Technology, Cambridge, Massachusetts, USA. ⁵SLAC National Accelerator Laboratory, Menlo Park, California, USA. ⁶Materials Science Division, Argonne National Laboratory, Lemont, Illinois, USA. ⁷X-ray Science Division, Argonne National Laboratory, Lemont, Illinois, USA. ⁸Department of Energy Conversion and Storage, Technical University of Denmark, Kongens Lyngby, Denmark. ⁹Present address: Research Laboratory of Electronics, Massachusetts Institute of Technology, Cambridge, Massachusetts, USA. ¹⁰Present address: Department of Applied Chemistry, Graduate School of Sciences and Technology for Innovation, Yamaguchi University, Tokiwadai, Japan. ¹¹Present address: Royal School of Mines, Imperial College London, South Kensington Campus, London, UK. ¹²These authors contributed equally: Reshma R Rao, Manuel J Kolb. ✉e-mail: reshmar@mit.edu; shaohorn@mit.edu

films in acid or base are facet-dependent^{23,24}, which has been correlated with adsorption energetics (for example, the metal–oxygen binding energy, $\Delta G_{\text{O}} - \Delta G_{\text{OH}}$)^{18,25,26}. Specifically, the redox peak just before the OER is shifted to more positive potentials for (101) compared with (110) and (100)^{27,28}, suggesting a weakening of the binding energy of the surface intermediates on (101).

In this study we aim to compare the electronic structure of Ru_{CUS} sites across these three surfaces, as well as the molecular details and energetics of adsorbates at potentials relevant to the OER in acid, to seek the physical origin of their activity differences. Density functional theory (DFT) results show that increasing the degree of undercoordination of the surface oxygen bonded to Ru_{CUS} and/or increasing the surface Ru–O–Ru bond angle on (100) and (101) can decrease the binding energy of OER-relevant intermediates. A decrease in the binding energy of the –OO group on the Ru_{CUS} of (100) relative to (110) is correlated with increased measured and computed intrinsic OER activity (where the deprotonation of –OO–H is rate determining); however, a further decrease in –OO binding on Ru_{CUS} of (101) results in the second water dissociation step ($-\text{O} + \text{H}_2\text{O} - (\text{H}^+ + \text{e}^-) \rightarrow -\text{OO}-\text{H}$) becoming rate determining, having measured and computed intrinsic OER activity that is lower than on the (100) surface. Such adsorbate intermediates on Ru_{CUS} of (100) and (101) are verified by synchrotron-based in situ surface X-ray scattering as a function of potential in acid, where the assignment of the nature of the proposed structures at potentials relevant to OER is aided by DFT calculations (similar to previous work¹⁸). Further evidence that the reaction mechanism at Ru_{CUS} catalyses the OER comes from in situ Fourier transform–infrared (FT–IR) spectroscopy detection of –OO-like species at OER-relevant potentials. Finally, such molecular details on the Ru_{CUS} site gained from single-crystal surfaces are used to explain the redox properties and OER activity of polycrystalline surfaces and nanoparticles.

Results

Surface-dependent electronic structure. First we consider the effect of the coordination of surface oxygen atoms on the surface electronic structure and adsorbate energetics of Ru_{CUS}. Although the (110) surface has both Ru_{CUS} and Ru_{BRI} sites, the (100) and (101) surfaces have only Ru_{CUS}. The Ru_{CUS} has a RuO₅ coordination with four neighbouring equatorial oxygen atoms and one apical binding site; however, the coordination of the equatorial oxygen atoms is different for the three surfaces. All four neighbouring equatorial oxygens on (110) are O_{3e}, whereas two of the four equatorial oxygen atoms that are bound to the Ru_{CUS} site on (100) and (101) are twofold-coordinated (O_{2c}), and the other two are O_{3e} (Fig. 1a,b). The Ru_{CUS} sites in (100) and (101), with undercoordinated equatorial oxygens, have an O_{2c} 2p band centre further away from the Fermi level (Fig. 1c,d and Supplementary Fig. 1) and stronger binding to equatorial oxygen (Ru_{CUS}–O_{2c}) compared with (110), which is in agreement with previous work on perovskites^{29,30}. This result is also in agreement with previous work of pseudo-valence charge-density analysis, showing that Ru_{CUS} on the (100) surface has different hybridization with surface oxygen than that of bulk ruthenium, whereas Ru_{CUS} on (110) surface does not exhibit this difference³¹. Consequently, Bader charge analysis of the Ru_{CUS} site shows that it is less oxidized for the (110) surface than the (100) and (101) surfaces, where the *d* band centre for the Ru_{CUS} sites scales with the Bader charge (Supplementary Tables 1 and 2 and Supplementary Fig. 3). Furthermore, (100) and (101) differ in the orientation of the polyhedra on the surface: two adjacent polyhedra with undercoordinated O_{2c} and Ru_{CUS} sites share an edge on the (100) surface (with a Ru_{CUS}–O_{2c}–Ru_{CUS} bond angle of 101°), whereas they share only a corner on the (101) surface (with a Ru_{CUS}–O_{2c}–Ru_{CUS} bond angle of 129°) for an ideal surface (Fig. 1b). Increasing this bond angle further lowers the oxygen 2p band centre from the Fermi

level and increases the Ru_{CUS}–O_{2c} bond strength (Fig. 1c,d and Supplementary Fig. 1). Stronger bonds between Ru_{CUS} and O_{2c} in the order (101) > (100) > (110) are accompanied by the Fermi level moving closer to the surface O_{1c} 2p band centre and a decrease in the binding energetics of Ru_{CUS} sites with apical adsorbates (for example, Ru_{CUS}–O_{1c}) in the trend of (110) > (100) > (101) (see Fig. 1d and Supplementary Fig. 2). This surface O_{1c} 2p band centre has recently been proposed as a site-specific descriptor of OER activity for a library of oxygen sites on a kinked RuO₂(121) surface from DFT studies³². Lowering the coordination of oxygen atoms bound to Ru_{CUS} from (110) to (100) decreases the binding energy of apical adsorbed oxygen (O_{1c}) by 0.04 eV. The influence of the surface Ru_{CUS}–O_{2c}–Ru_{CUS} bond angle is more substantial, where increasing the angle from 101° on (100) to 129° on (101) decreases the oxygen (O_{1c}) binding energy by 0.14 eV. The local coordination of equatorial oxygen for Ru_{CUS} thus results in a change in the electronic structure and binding energetics of apical adsorbates on Ru_{CUS}, with the binding energy decreasing in the order (110) > (100) > (101).

Surface-dependent reaction energetics of OER. We computed the free energies of OER intermediates on different Ru_{CUS} sites of RuO₂(100) and (101) surfaces and compared them with the (110) surface¹⁸. A four proton–electron concerted process for the OER—involving six intermediates, as reported previously for the (110) surface¹⁸—is shown in Fig. 2 and Supplementary Table 3. The process starts with an empty Ru_{CUS} (step 1) on an otherwise oxygenated surface. Water adsorbs apically on Ru_{CUS} (2) and is deprotonated successively to form –OH (3) and –O (4) species. Subsequently, a second water molecule adsorbs and is deprotonated to form an –OOH group (5), which is unstable and donates its proton to a neighbouring oxygen site to form an –OO species (6) (Supplementary Fig. 4). The proton of the –OOH group is transferred barrierlessly when the initial configuration of the DFT calculation is the one in which the –OOH group points to a neighbouring oxygen site. The species thus formed is similar in nature to a negatively charged species, –OO[–], which is based on the O–O bond length of ~1.28 Å and can thus interact strongly with a neighbouring proton (Supplementary Table 4). The removal of the proton-stabilizing –OO species results in the release of molecular oxygen (7). Steps from the formation of –O (4) to the release of molecular oxygen (7) on Ru_{CUS} could be uphill at 1.5 V_{DFT-RHE}. The oxygen (4) and proton-stabilized –OO intermediate (–OO–H) (6) binding on Ru_{CUS} decreases from (110) > (100) > (101). The binding energy for –O (4) on the Ru_{CUS} sites of (100) and (101) was weakened by 0.04 and 0.18 eV, respectively, whereas that of proton-stabilized –OO (6) on the Ru_{CUS} sites of (100) and (101) was weakened by 0.15 and 0.34 eV, respectively, relative to (110). On the other hand, –OH had the same binding energy for (100) and (101) and was found to be only 0.04 eV more stable on (110). As proton-stabilized –OO (6) was weakened more greatly than that of –O (4) on the Ru_{CUS} site of (100) relative to (110), the RDS involving the removal of the final proton-stabilizing –OO intermediate for (110)¹⁸ was found to be isoenergetic with the –OOH formation step (within the uncertainty of DFT) for the (100) surface (Fig. 2). However, further decreasing the binding energy of the stabilized –OO intermediate and simultaneously weakening –O species on the Ru_{CUS} site of (101) changes the OER RDS to the dissociation of the second water molecule on a fully oxidized surface ($-\text{O} + \text{H}_2\text{O} - (\text{H}^+ + \text{e}^-) \rightarrow -\text{OO}-\text{H}$). These DFT-calculated energetics suggest that, on the basis of reaction free energies (that is, excluding additional kinetic barriers), different surface adsorbates should be stabilized on the Ru_{CUS} site at 1.5 V_{DFT-RHE}, where the (100) surface could have –O or –OO species and the (101) surfaces should have –O species. Under oxygen evolution potentials (>1.5 V_{RHE}), when all steps are thermodynamically downhill, additional kinetic barriers may exist, as calculated in the recent work of Dickens et al.³³. However, based on the Brønsted–Evans–Polanyi

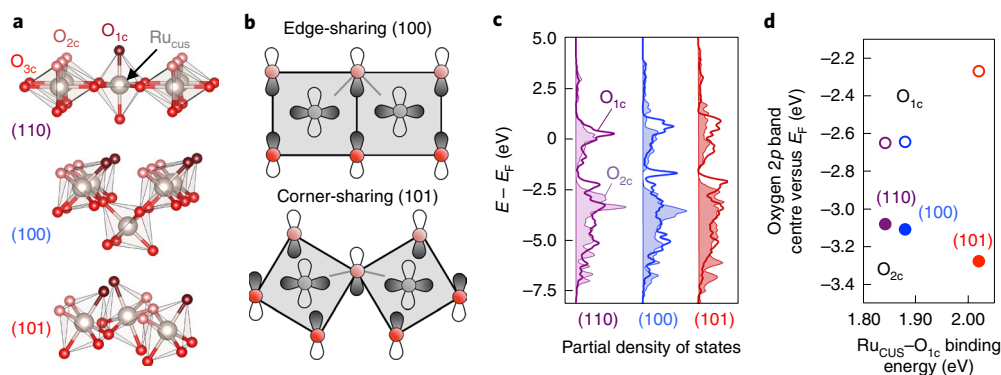


Fig. 1 | The coordination and electronic structure of surface ruthenium and oxygen atoms on different facets of RuO₂. **a**, Schematics depicting the arrangement of undercoordinated ruthenium (Ru_{CUS}, grey), undercoordinated bridging oxygen (O_{2c}, pink), adsorbed oxygen (O_{1c}, dark red) and fully coordinated bulk oxygen (O_{3c}, red) sites for the different surfaces. The Ru_{CUS} site on the (110) facet is coordinated to zero O_{2c} atoms, whereas it is coordinated to two O_{2c} atoms for the (100) and (101) facets. **b**, Schematics of the equatorial plane of the (100) and (101) surfaces. The octahedra share an edge for the (100) surface and a corner for the (101) surface, forming a larger Ru_{CUS}-O_{2c}-Ru_{CUS} bond angle of 129° in contrast to 101°. The larger bond angle allows for a higher orbital overlap between Ru_{CUS} and O_{2c}. **c**, The electron density of states for the oxygen 2p orbitals of the O_{2c} atoms (shaded) on a stoichiometric surface (no O_{1c} atoms) and for the O_{1c} atoms on a fully oxidized surface. **d**, The oxygen 2p band centre for the O_{2c} bridging oxygen (closed points) is lowered with an increase in the number of undercoordinated O_{2c} oxygen atoms bonded to Ru_{CUS} and the Ru_{CUS}-O_{2c}-Ru_{CUS} bond angle. By principle of bond order conservation, the O_{1c} oxygen 2p band centre (open points) increases with a decrease in the O_{2c} 2p band centre, which is accompanied by a weaker Ru_{CUS}-O_{1c} binding energy. The ruthenium 4d density of states is shown in Supplementary Fig. 1, whereas the Bader charges are shown in Supplementary Fig. 3 and Supplementary Tables 1 and 2.

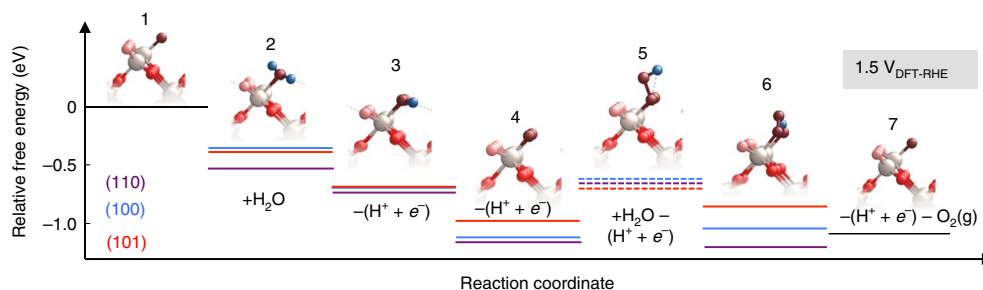


Fig. 2 | A DFT-calculated reaction free energy diagram at 1.5 V_{DFT-RHE}. A DFT-calculated free energy diagram for the OER mechanism at 1.5 V_{DFT-RHE} (Supplementary Tables 3, 15 and 16), showing the six possible intermediates for the (110) (ref. 18), (100) and (101) surfaces. The dashed lines indicate unstable -OOH precursor states, which are needed for -OO-H formation. The schematics for the intermediates on the (100) surface are shown. Grey, ruthenium; blue, hydrogen; dark red, O_{1c}; pink, O_{2c}; red, O_{3c}.

relationship³⁴, we expect that these kinetic barriers will scale with the reaction free energies presented here. This notion is supported by the correlation between the experimental and thermodynamic overpotential plotted in Fig. 2.

Operando X-ray scattering of RuO₂(100) and (101). Operando synchrotron-based surface X-ray scattering crystal truncation rod (CTR) analysis coupled with DFT computation was used to reveal adsorbates on Ru_{CUS} for the surface of single crystals with the (100) and (101) termination in 0.1 M HClO₄. Here the surface normal is referred to as the (001) direction and the two in-plane directions as (100) and (010) for all of the surface orientations. Surface diffraction data exhibited distinct changes in the anti-Bragg region for the (10L) rod (at Miller index values of $L=1.5, 3.5$ for (100) (Fig. 3a–c), and at $L \approx 1.5$ for (101) (Fig. 4a–c) at 1.0 V_{RHE}, 1.3 V_{RHE} and 1.5 V_{RHE}. The other specular and off-specular rods for the (100) (Supplementary Fig. 5) and (101) (Supplementary Fig. 6) surfaces showed no distinct changes as a function of potential, confirming that the surface does not undergo any reconstruction or roughening during the course of the measurements (~10 h). This is also consistent with our previous work¹⁹ showing that terrace sites are

not as prone to dissolution as highly undercoordinated defect sites, resulting in a Faradaic efficiency of dissolution of ~0.02% for single-crystal surfaces (with a corresponding s number, defined as the number of oxygen molecules evolved per dissolved ruthenium³⁵, of ~5,000). Detailed surface models to fit the specular and off-specular data, fitting constraints and results and sensitivity of fit analysis are shown in Supplementary Note 3. Inferences about the nature of the oxygenated species were made based on the fitted bond length between the Ru_{CUS} site and adsorbed oxygen atoms. In addition, DFT was used to compute the energetics of different surface structures as a function of potential (Supplementary Tables 15 and 16). By considering the surface structure with the lowest Gibbs free energy in a given potential window from DFT and the Ru_{CUS}-O distance detected for the (100) and (101) surfaces at 1.0 V_{RHE}, 1.3 V_{RHE} and 1.5 V_{RHE}, molecular descriptions of surface adsorbates on Ru_{CUS}—that are compatible with both the DFT and model-based fitting of experimental surface diffraction spectra—were proposed.

The bond length between Ru_{CUS} and apically adsorbed oxygenated (Ru_{CUS}-O_{1c}) species for the (100) surface decreased markedly from 2.85 Å at 1.0 V_{RHE} to 2.00 Å at 1.3 V_{RHE}, whereas the bond length between Ru_{CUS} and undercoordinated equatorial oxygen

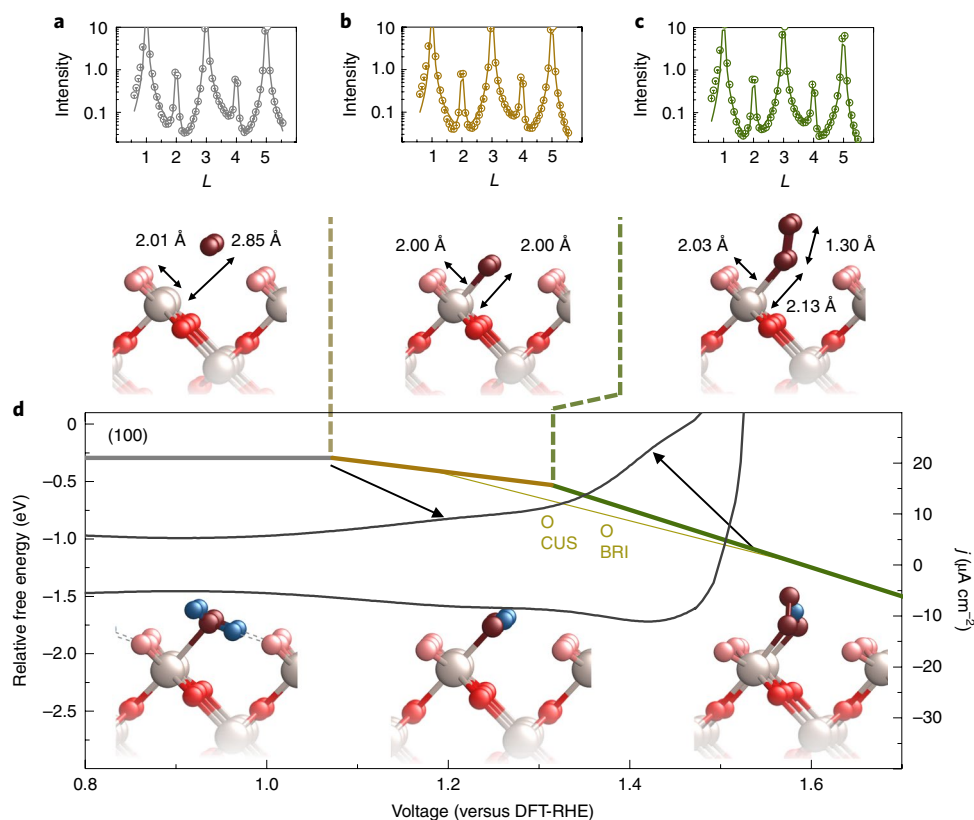


Fig. 3 | Potential-dependent surface structures for RuO₂(100). **a–c**, The (10L) rod (other rods can be found in Supplementary Fig. 5) measured for the (100) surface at 1.0 V_{RHE} (**a**), 1.3 V_{RHE} (**b**) and 1.5 V_{RHE} (**c**) shows changes in the symmetry of the intensities about the Bragg peak $L = 2$ as a function of potential. Structures corresponding to the experimentally fitted data show a decrease in the Ru_{CUS}–O_{1c} bond length from 1.0 V_{RHE} to 1.3 V_{RHE}, with the formation of an –OO species at 1.5 V_{RHE}. Fitted parameters and results are shown in Supplementary Tables 5–8, and bond lengths with error bars are shown in Supplementary Table 9. **d**, A DFT-generated diagram that shows the relative Gibbs free energies of the most stable adsorbate configurations as a function of electrochemical potential (Supplementary Table 15 shows the computed free energy of all surface structures considered). The transition from one structure to another is representative of an experimentally observed redox transition. At low potentials, water is stabilized on the Ru_{CUS} site, which is deprotonated to form –OH at ~ 1.05 V_{DFT-RHE} and subsequently deprotonated to form –O. At 1.5 V_{DFT-RHE} an –OO group is stabilized on the Ru_{CUS} site by an –OH group on a neighbouring Ru_{BRI} or Ru_{CUS} site, with these two configurations being energetically degenerate. An experimental cyclic voltammogram (grey curve) of the (100) facet measured at 50 mV s^{–1} in argon-saturated 0.1 M HClO₄ is shown for reference. Black arrows link the DFT-predicted redox transitions to experimentally observed redox peak positions.

(Ru_{CUS}–O_{2c}) remained unchanged (within the experimental and modeling uncertainty) from 1.0 V_{RHE} to 1.3 V_{RHE} (~ 2.00 Å; Fig. 3a,b). This change can be attributed to the dissociation of the adsorbed –H₂O to form –OH on Ru_{CUS}, which is in agreement with DFT results that show the deprotonation of adsorbed –H₂O on Ru_{CUS} at potentials greater than ~ 1.05 V_{DFT-RHE} (Fig. 3d). This assignment is further supported by the reasonably good agreement between the experimental redox peak at ~ 1.2 V_{RHE} (grey curve, Fig. 3d) and the corresponding DFT-computed potential at ~ 1.05 V_{DFT-RHE}. This difference between experimental and theoretical redox potentials is within the range of values previously reported for rutile IrO₂ (ref. 25) and RuO₂ (ref. 11), possibly due to uncertainties in the calculations. By contrast, the Ru_{CUS}–O_{1c} bond lengths for (101) were comparable at 1.0 and 1.3 V_{RHE} (2.04 Å and 1.99 Å, respectively). The Ru_{CUS}–O_{2c} bond length changed from 2.01 Å at 1.0 V_{RHE} to 1.99 Å at 1.3 V_{RHE} (Fig. 4a,b). As the bond length of O_{1c} with Ru_{CUS} is larger than bulk apical Ru–O bond (1.905 Å), but shorter than computed Ru_{CUS}–O bond for adsorbed water (~ 2.26 Å)²², we propose that Ru_{CUS} is filled with an –OH group at 1.0 V_{RHE} and 1.3 V_{RHE}. DFT calculations show the deprotonation of the equatorial bridging oxygen O_{2c} occurs at ~ 1.0 V_{DFT-RHE} while the Ru_{CUS} site remained filled with –OH (Fig. 4d). The experimental redox transition for this facet is not well defined but occurs over a broad range from ~ 1.05 V_{RHE} to ~ 1.25 V_{RHE}

(grey curve, Fig. 4d), which is in agreement with the predicted transition potential by DFT. Our results show that, irrespective of the water dissociation tendency on Ru_{CUS} at 1.0 V_{RHE} (undissociated on (100), partially dissociated on (110) and fully dissociated on (101)), all three facets were found to have –OH on Ru_{CUS} and a fully oxygenated equatorial O_{2c} site at 1.3 V_{RHE} (see Supplementary Fig. 19–21 for a comparison of bond lengths and angles).

Further increasing the potential to 1.5 V_{RHE} resulted in a surface structure where an –OO was present on the Ru_{CUS} site of the (100) surface, as has been reported recently for (110)¹⁸ (Fig. 3c), and on IrO₂(110)³⁶, which is in agreement with DFT results showing proton-stabilized –OO species at 1.5 V_{DFT-RHE} (Figs. 2 and 3d). The assignment is further supported by the experimentally observed redox peak at ~ 1.45 V_{RHE}, just before the onset of OER and also in agreement with previous X-ray absorption spectroscopy results on RuO₂ particles, where a downshift in the whiteline of the ruthenium L -edge was observed before the OER, supporting the formation of an –OOH like species³⁷. We note that without the presence of an –OO group on the Ru_{CUS} of the (100) surface, a structure with a short Ru_{CUS}–O_{1c} bond length of 1.68 Å and a larger figure of merit is obtained (0.113), compared with the best-fit solution (0.087) with the –OO group (Supplementary Fig. 14). Unlike (110) and (100), a completely oxidized surface was detected on the (101) surface at

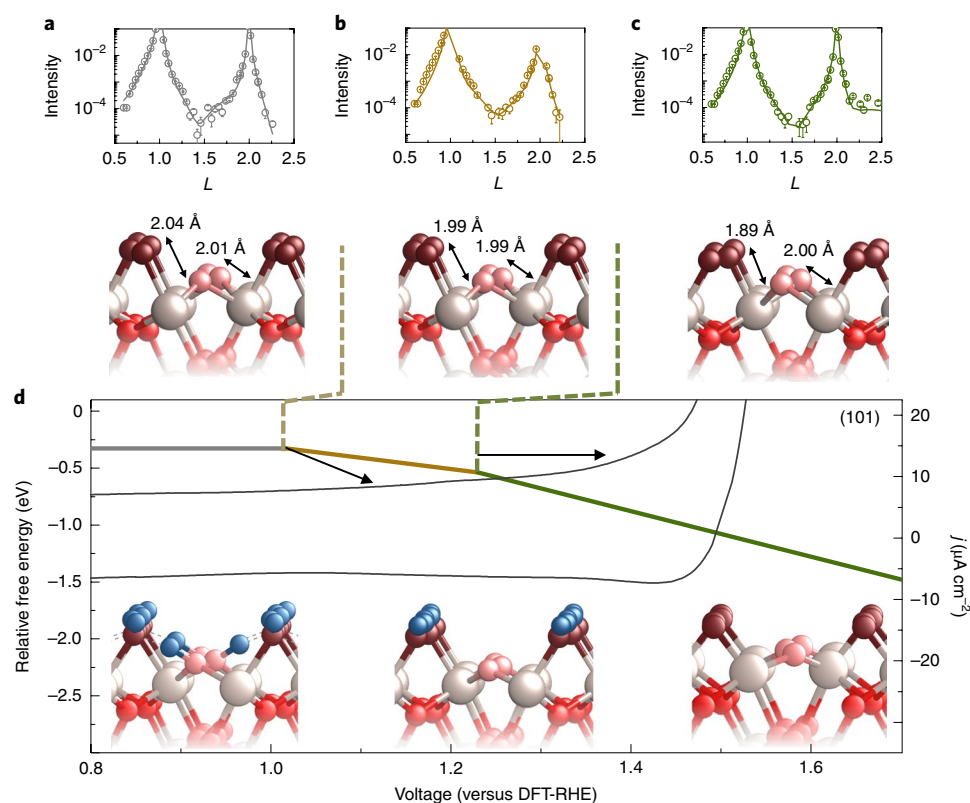


Fig. 4 | Potential-dependent surface structures for RuO₂(101). **a–c**, The (10L) rod (other rods in Supplementary Fig. 6) measured on the (101) surface at 1.0 V_{RHE} (**a**), 1.3 V_{RHE} (**b**) and 1.5 V_{RHE} (**c**) shows changes in the shape of the anti-Bragg position at $L \approx 1.5$. Structures corresponding to the experimentally fitted data show a decrease in the Ru_{CUS}–O_{1c} bond length from 1.0 V_{RHE} to 1.5 V_{RHE}. Fitted parameters and results are shown in Supplementary Tables 11–13 and bond lengths with error bars are shown in Supplementary Table 14. **d**, A DFT-generated diagram showing the relative Gibbs free energy of the most stable adsorbate configurations as a function of electrochemical potential (Supplementary Table 16 shows the computed free energy of all surface structures considered). The energetics of different adsorbates for the (101) facet suggests the presence of an –OH group on the Ru_{CUS} site with a protonated bridging oxygen at 1.0 V_{DFT-RHE}. Increasing the potential results in the deprotonation of the bridging oxygen and further increasing the potential to 1.5 V_{DFT-RHE} results in a deprotonation of the –OH group on the Ru_{CUS} site to form –O. An experimental cyclic voltammogram (grey curve) of the (101) facet measured at 50 mV s⁻¹ in argon-saturated 0.1 M HClO₄ is shown for reference. Black arrows link the DFT-predicted redox transitions to experimentally observed redox peak positions.

1.5 V_{RHE}. The Ru_{CUS}–O_{1c} bond length was found to be 1.89 Å, which is 0.1 Å lower than that found at 1.3 V_{RHE}, whereas the distance to undercoordinated equatorial oxygen is unchanged from the value at 1.3 V_{RHE} (2.00 Å) (Fig. 4c). This experimental finding is in agreement with our DFT results showing a fully oxidized surface structure at 1.5 V_{DFT-RHE} (Fig. 4d). The weaker adsorption of –O and –OOH on the Ru_{CUS} site of (101) compared with (110) and (100) changed the RDS to $(-O + H_2O - (H^+ + e^-) \rightarrow -OO-H)$, which validates the fully oxidized surface measured at 1.5 V_{RHE}. Although our DFT results predict that the redox transition corresponding to deprotonation of –OH on Ru_{CUS} to form –O occurs at ~ 1.22 V_{DFT-RHE}, experimentally, a fully hydroxylated Ru_{CUS} was detected at 1.3 V_{RHE} for the (101) surface. On the basis of our experimental findings from (1) CTR, which suggest a surface structural transition between 1.3 V_{RHE} and 1.5 V_{RHE} and (2) the experimental cyclic voltammogram, which shows a redox transition at ~ 1.45 V_{RHE}, we rationalize that the discrepancy between experimental and DFT redox transition potentials results from a too strong binding of oxygen predicted by DFT on (101). Our results therefore revealed that decreasing the binding energy on Ru_{CUS} from (110) and (100) to (101) resulted in a completely oxidized surface as opposed to an –OO-covered surface, which corresponds to a change in the RDS for OER (Fig. 2).

Surface-dependent OER activity of Ru_{CUS}. Experimentally obtained OER currents were found to increase from (110), (101) to (100)

(as demonstrated in Fig. 5a (in 0.1 M HClO₄) and Supplementary Fig. 22 (in 1 M HClO₄)). We note that no strong pH dependence was observed and the OER activity trends observed at room temperature and in 0.1 M HClO₄ are valid at lower pH and temperatures of up to 45 °C. The measured OER activity—defined as the current density measured at 1.53 V_{RHE} and 1.60 V_{RHE}—exhibits a volcano trend with decreasing computed binding energy of –O (step 4 in Fig. 2) on Ru_{CUS} (Fig. 5b). These results are corroborated with the predicted OER activity, defined by the overpotential, above which all of the steps will be downhill energetically. The free energy change for steps 6 to 7 ($-OO-H - (H^+ + e^-) \rightarrow O_2 + *$) decreases with weakening of the adsorbed apical binding on Ru_{CUS} from the (110) to (100) surface but a further decrease in the binding strength from (100) to (101) makes steps 4 to 6 ($-O + H_2O - (H^+ + e^-) \rightarrow -OO-H$) uphill in free energy (Fig. 2). The computed overpotential was found to decrease from 0.38 V on Ru_{CUS} of (110) to 0.34 V on (100) and then increase to 0.39 V on (101) at 1.5 V_{DFT-RHE}. A decrease in the computed overpotential by 40 mV from (110) to (100) is in qualitative agreement with a one order of magnitude increase in activity at 1.6 V_{RHE}, considering a measured Tafel slope of 60 mV per decade. On the other hand, although the Ru_{CUS} of (101) was found to have the largest overpotential from DFT, experiments showed an intermediate activity between the (110) and (100) surfaces. The higher activity found experimentally for the Ru_{CUS} of (101) can be attributed to the greater roughness

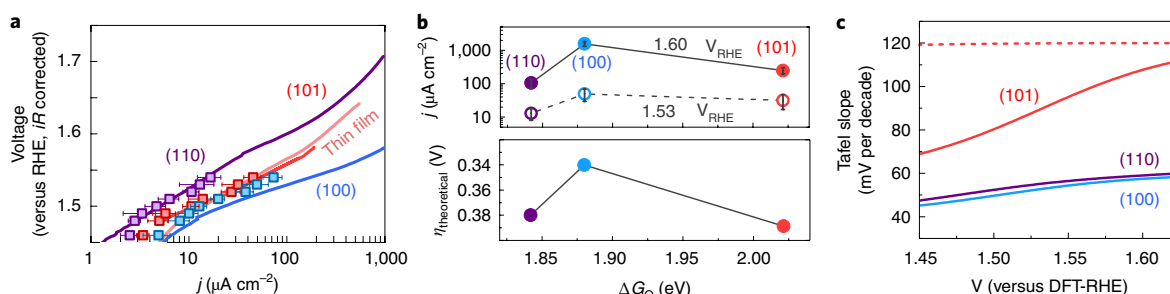


Fig. 5 | Surface-dependent water oxidation kinetics on RuO₂. **a**, Tafel plots of OER activities in O₂-saturated 0.1 M HClO₄ (data for 1 M HClO₄ in Supplementary Fig. 22), measured by cyclic voltammetry at 10 mV s⁻¹ (averaged forwards and backwards, lines) and potentiostatic measurements (constant applied voltage, points). The Tafel slopes for all of the surfaces between 1.5 V_{RHE} and 1.6 V_{RHE} are ~60 mV per decade **b**, The current density at 1.53 V_{RHE} (potentiostatic measurements) and 1.60 V_{RHE} (capacitance corrected cyclic voltammetry) show that the highest OER activity is obtained for the (100) surface. The error bars are obtained from the s.d. of three independent measurements. The theoretical overpotential as a function of the binding energetics of the -O intermediates. Weakening the Ru_{CUS}-O_{1c} binding energy reduces the energetic barrier for -OO-H - (H⁺ + e⁻) → O₂ + * (from (110) to (100)); a further decrease in the binding energy leads to a change in the RDS for the (101) surface to -O + H₂O - (H⁺ + e⁻) → -OO-H, with an increase in the theoretical overpotential. **c**, Predicted Tafel slopes as a function of the potential that results from a difference in coverage of intermediate species before the RDS (Supplementary Table 17 shows the mathematical equations used to obtain the Tafel slopes). The dashed line for the (101) facet represents the values predicted from DFT alone, whereas the solid line for the (101) facet represents the values obtained after accounting for the discrepancy of redox transitions between the theoretically obtained free energy diagrams and experimental cyclic voltammograms.

of this surface (~2–3 Å), as evidenced by the sharper decay in the CTR signal from the Bragg peak to the anti-Bragg position in the specular rod than the (100) (Supplementary Fig. 5) and (110)¹⁸ surfaces (Supplementary Fig. 6, Supplementary Tables 11–13), which may expose different sites that have improved binding energetics for the OER intermediates. The volcano trend between thermodynamic binding energetics and the OER activity in this study contrasts with recently reported results on RuO₂(110), where the binding energy of oxygen on the Ru_{CUS} site was altered (measured experimentally by changes in the redox peak positions) by changing the solution pH²⁶. These differences could be attributed to the influence of pH and cations on the reaction mechanism and barriers in addition to differences in binding energy of intermediates^{38,39}, which is supported by our previous work on oriented RuO₂ surfaces in alkaline solutions which show non-Nernstian pH dependence of redox peak position and the OER activity²⁷.

Experimentally measured Tafel slopes of the OER on (110), (100) and (101) surfaces are in agreement with the energetics of reaction intermediates obtained from DFT. The experimentally measured Tafel slope in the range of 1.5–1.6 V_{RHE} was found to be ~60 mV per decade for all of the three surfaces (Fig. 5a), which is consistent with previous experimental work on highly oriented thin films and polycrystalline RuO₂ surfaces^{5,23}, and estimated Tafel slopes from the reaction mechanism obtained by DFT (Fig. 2) in this study. The Tafel slope was estimated to be^{40,41} $60/\alpha$ mV per decade, where α is the transfer coefficient can be given by $\alpha = \frac{n_f}{\nu} + n_r\beta$, where n_f is the number of electrons transferred per Ru_{CUS} site in the step before the RDS in the voltage range of Tafel analysis, ν is the number of times the RDS occurs for one repetition of the overall cycle (equal to 1 for the OER on all three RuO₂ surfaces), β is the symmetry factor (assumed to be 0.5, supported by previous experimentally fitted values for RuO₂(110) single crystals at potentials over 1.52 V_{RHE}; (ref. 42)) and n_r is the number of electrons in each occurrence of the RDS⁴³ (equal to 1 for OER on all three RuO₂ surfaces; Fig. 2). As DFT predicts that removing the proton stabilizing the -OO on Ru_{CUS} was the RDS for the OER on the (110) and (100) surfaces (Fig. 2), the step before RDS, that is the water dissociation on a fully oxidized surface followed by electron-coupled deprotonation, -O + H₂O → -OO-H + (H⁺ + e⁻) was used to determine the coverage of -O and -OOH on Ru_{CUS} as a function of voltage (more specifically, ΔG_{OOH} and ΔG_{O} , see the Methods section and

Supplementary Note 6 for more details). Having n_r equal to θ_{O} on Ru_{CUS} results in Tafel slopes varying from ~50 to ~60 mV per decade for (110) in purple and (100) in blue in the voltage range from 1.45 to 1.60 V_{DFT-RHE} (Fig. 5c), in agreement with experimental data (Fig. 5a). Recent work³³ on the RuO₂(110) surface also related the change in the Tafel slope to the change in the surface coverage; however, their DFT and microkinetic model suggested that the formation of -OOH was rate-limiting and the surface was covered with -OH below ~1.5 V_{RHE} (corresponding to a Tafel slope of 39 mV per decade) and covered with -O at higher potentials (corresponding to a Tafel slope of 120 mV per decade). By contrast to the (110) and (100) surfaces, our DFT studies predict a completely oxygenated Ru_{CUS} at potentials greater than 1.2 V_{DFT-RHE} for (101), where all Ru_{CUS} sites are at RDS, resulting in n_r of zero and Tafel slope of 120 mV per decade in the potential range (dashed line in Fig. 5c). Considering that CTR for (101) at 1.3 V_{RHE} showed Ru_{CUS} filled with -OH (full coverage) and became deprotonated at 1.5 V_{RHE}, we lowered the computed binding energy of -O by 0.15 eV to match the experimental redox transition (Fig. 4), which resulted in Tafel slopes increasing from ~70 to ~110 mV per decade from 1.45 to 1.625 V_{DFT-RHE}, in an increased agreement with the experimentally observed Tafel slope (~60 mV per decade), shown as red solid line in Fig. 5c.

Further evidence for the involvement of -OO species in the RDS of the OER came from surface-enhanced infrared absorption (SEIRA) spectroscopy measurements on a polycrystalline RuO₂ thin film, as shown in Fig. 6a and Supplementary Figs. 23–26. Below 800 cm⁻¹, the signal was dominated by strong absorption from the silicon prism. On increasing the voltage from 0.5 V_{RHE}, two peaks at ~1,100 cm⁻¹ and ~1,000 cm⁻¹ were observed, which could be attributed to the Si-O-Si prism⁴⁴ and perchlorate ions at the interface⁴⁵, respectively. At 1.5 V_{RHE} and higher, a third peak at ~899 cm⁻¹ appeared. The -OO group on the Ru_{CUS} site that is stabilized by an -OH group on the neighbouring bridge site for (110)¹⁸ and (100), revealed by CTR and DFT (Fig. 3), is predicted to have an infrared active vibration mode at 910 cm⁻¹ for an -OO coverage of 0.5, or at 889 cm⁻¹ if every Ru_{CUS} is considered to have an -OO group from DFT (Supplementary Table 18). The peak detected at ~899 cm⁻¹ at OER-relevant potentials can therefore be attributed to proton-stabilized -OO species on a polycrystalline RuO₂ surface. This assignment is further supported by measurements in deuterated solutions that reveal a shift in the frequency to

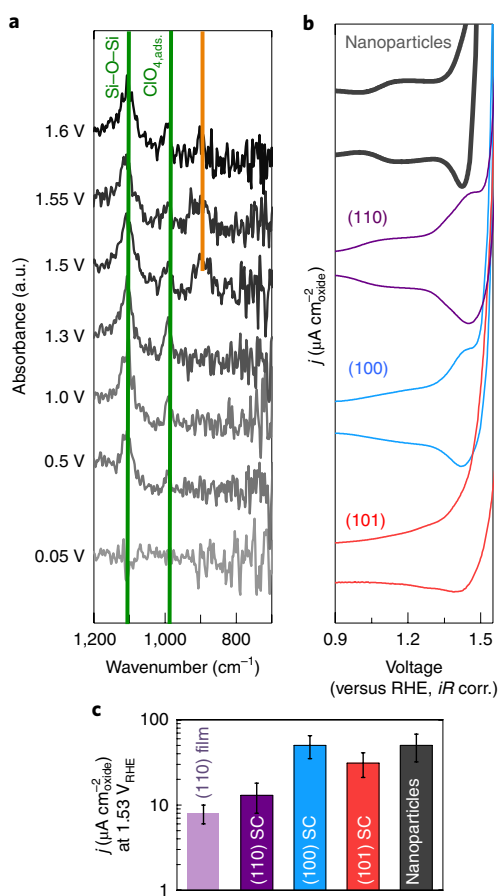


Fig. 6 | The reaction mechanism and water oxidation activity on polycrystalline RuO₂ surfaces. **a**, A SEIRA spectra for a polycrystalline RuO₂ surface (Supplementary Fig. 26 shows results in deuterated solutions). Si-O-Si (ref. 44) and adsorbed perchlorate ion⁴⁵ peaks are present irrespective of potential. At potentials higher than 1.50 V_{RHE}, an additional peak appears at -899 cm⁻¹ that corresponds to the formation of an -OO group on the Ru_{CUS} site, interacting with a neighbouring protonated bridging oxygen (Supplementary Table 18 lists the theoretical frequency for all structures considered). **b**, A comparison of the cyclic voltammograms of RuO₂ nanoparticles to oriented single-crystal surfaces. Measurements were made in argon-saturated 0.1 M HClO₄ at 50 mV s⁻¹. **c**, A comparison of the OER activity at 1.53 V_{RHE} between (110) thin films²⁶ (extrapolated on the basis of data from 1.55–1.65 V_{RHE}, assuming a constant Tafel slope), (110), (100) and (101) single crystals (SCs), and the nanoparticles reported here (Supplementary Fig. 28 shows a Tafel plot of the activity between 1.45 V_{RHE} and 1.65 V_{RHE} (all measured in 0.1 M HClO₄)). The error bars are obtained from the s.d. of three independent measurements.

815 cm⁻¹, confirming the strong interaction of the -OO group with a neighbouring hydrogen/deuterium atom (Supplementary Fig. 26, Supplementary Table 18).

Implications for RuO₂ nanoparticles. Single-crystal RuO₂(110) (ref. 18), thin films of RuO₂(110) grown using molecular beam epitaxy²⁶ and single-crystal RuO₂(100) exhibit a redox peak at ~1.2 V_{RHE} in 0.1 M HClO₄ (Fig. 6b), which can be attributed to deprotonation of adsorbed water to form -OH (Fig. 3), whereas the redox peak at ~1.45 V_{RHE} can be attributed to the adsorption and dissociation of water onto a fully oxidized surface followed by electron-coupled deprotonation to form proton-stabilized -OO (Fig. 3). These two redox transitions were also observed on RuO₂ nanoparticles (Sigma-Aldrich, ~25 nm; X-ray diffraction and transmission

electron microscopy characterization in Supplementary Fig. 27) in Fig. 6b, which indicates that Ru_{CUS} sites from (110) and (100) govern the redox transitions or pseudo-capacitance of RuO₂ nanoparticles. Furthermore, the OER activities of RuO₂ nanoparticles measured in this study (Supplementary Fig. 28) and in previous work^{5,19} are comparable to RuO₂(100) and (101) but are around five times higher than that of single-crystal¹⁸ and thin-film²⁶ RuO₂(110), as shown in Fig. 6c. Although some RuO₂ polycrystalline thin films⁴⁶ and nanoparticles⁴⁷ thermally annealed at temperatures lower than 600 °C have considerably higher OER activity than these RuO₂ single-crystal surfaces, they are not included in the discussion and comparison here as they have more structural defects that are evidenced by broad X-ray diffraction^{46,47}. Their stability during the OER over time is also not known, considering that the contribution from the dissolution of ruthenium to the measured OER current increases with lowering the annealing temperature of RuO₂ (ref. 19). Our results therefore suggest that the OER activity of highly crystalline RuO₂ nanoparticles might be governed by RuO₂(100) and (101) surfaces at OER-relevant potentials. This is also in agreement with previous theoretical work that shows that facets other than the (110) surface govern the activity of the OER at high potentials^{48,49}.

Conclusions

In this study, by combining CTR and DFT, we discuss the role of surface-dependent Ru_{CUS} (that is, the active site) in governing the OER reaction mechanism and consequently the overall OER activity. Although (110), (100) and (101) all have Ru_{CUS} sites in the same RuO₅ coordination, with four neighbouring equatorial oxygen atoms and one apical binding site, the coordination of the equatorial oxygen atoms and the bond angle between Ru_{CUS} sites and undercoordinated equatorial oxygen is different, resulting in different energetics of -O and proton-stabilized -OO for apical binding with a decreasing order from (110), (100) to (101). DFT results show that reducing the binding of the proton-stabilized -OO group on the Ru_{CUS} site of (100) relative to (110) lowers the energetic barrier of electron-coupled deprotonation from the -OO-H group (the RDS), leading to a greater predicted OER activity for the Ru_{CUS} site of (100). On the other hand, further weakening of the binding energy on the Ru_{CUS} site of (101) results in the RDS changing to the second water dissociation step on a fully oxidized surface to form a proton-stabilized -OO species, leading to a lower predicted OER activity for the Ru_{CUS} site of (101) relative to (100) and (110). The surface-dependent adsorbates on Ru_{CUS} at the OER-relevant potentials (as predicted by DFT) were consistent with best-fit surface models obtained from operando surface diffraction measurements. The Ru_{CUS} site of (100) has -H₂O and -OH adsorbed at 1.1 and 1.3 V_{RHE}, respectively, whereas the Ru_{CUS} site of (101) has -OH at both voltages. At an OER-relevant potential of 1.5 V_{RHE}, a combination of DFT and surface diffraction measurements points to an -OO group on the Ru_{CUS} site of (100) (similar to the Ru_{CUS} site of (110)), but an oxygen-terminated surface for the Ru_{CUS} site of (101), and this difference is in agreement with the predicted change in the RDS for different Ru_{CUS} sites from DFT. Further evidence of -OO species that are involved in the RDS for the OER comes from SEIRA spectroscopy measurements on polycrystalline RuO₂, where we note a vibration mode that corresponds to an -OO intermediate on Ru_{CUS}. Such mechanistic insights, as well as computed and experimental OER activities of the Ru_{CUS} sites from different single-crystal facets, explain the redox properties and OER activities of highly crystalline RuO₂ nanoparticles. Directly tuning the electronic structure of surface active sites while maintaining the bulk chemistry opens up new directions in OER catalyst design; for example, understanding the effect of surface crystallographic orientation on the OER activity enables rational design of nanoparticle shapes, where the work of Wang et al.⁴⁸ demonstrates the tunability of Wulff particle shapes for RuO₂ surfaces. Further studies are needed to understand how the active site can be further altered by

systematic control of different defects, which can create Ru–O surface coordination environments that are considerably different from the Ru_{CUS} sites of (110), (100) and (101), leading to much greater OER activity^{32,50}. Moreover, the coordination environment of the active site can also be altered to tune the binding energetics on the active site by cation^{51–53} and/or anion⁵⁴ doping of atoms in the first or second coordination shell of active ruthenium sites, and also by creating different defect sites with unique Ru–O surface coordination environments^{32,50} by (electro)chemical treatments. Even more tunability in the coordination environment of surface ruthenium sites can be achieved by designing molecular ruthenium-based chemistries. Here the ligand environment can not only alter the binding energetics of the OER intermediates, but the degree of interaction of these ligands can also modify the Ru–Ru distance to allow for an oxygen coupling mechanism between adsorbed oxygens on two adjacent sites⁵⁵, which doesn't require the formation of an –OOH species that results in an energetic penalty for the overall reaction. A molecular understanding of the influence of the local environment of an active site on the OER reaction mechanism and activity can enable the design of catalysts that surpass the highest activity predicted by traditional bulk electronic structure descriptors.

Methods

Electrochemistry. Single-crystal RuO₂ surfaces were synthesized by oxidative evaporation/redeposition of RuO₂ powders as described in refs.^{56,57}. The as-grown crystals exhibited few defects, such as twinning or faults, and had a bulk mosaic within ~0.01° of the perfect crystal and exposed surfaces of (110), (100) and (101) that ranged from ~2 mm to 5 mm in size. Furthermore, a bulk crystal was cut by the Princeton Scientific Corporation to expose a (001) facet to an orientation accuracy <0.1° and polished to a roughness <10 nm. Electrical contacts were applied to the back of the crystal, which was mounted in a Teflon mold (FEP 100, DuPont) with the facet under consideration exposed to the electrolyte. For the (101) surface, an epitaxial thin film prepared using pulsed laser deposition (as described in ref.²⁸) was also used. Nanoparticles were purchased commercially (Sigma-Aldrich, 99.99% trace metal base). The particle-based film electrodes were prepared by slowly drying catalyst ink prepared using 4 mg acetylene black carbon, 20 mg RuO₂, 0.12 ml 3.33wt% Nafion solution and 3.88 ml tetrahydrofuran; 10 μl ink (equivalent to 0.050 mg_{oxide}) was dropcast onto a glassy carbon rotating disk electrode (Pine Instrument). A Biologic SP-300 potentiostat and standard three-electrode set-up was used. For each measurement, ~120 ml of 0.1 M HClO₄ (70% Veritas double distilled) was prepared using deionized water (Millipore, >18.2 MΩ cm) and presaturated with argon for 60 min to prevent reduction of oxygen at low potentials; argon gas was also left bubbling throughout the measurement. Activity measurements were made in O₂-saturated solutions. A 4 M saturated Ag/AgCl electrode (Pine) was used (calibrated to the RHE scale) and a large platinum wire was used as the counter electrode. Cyclic voltammetry measurements were performed at 50 mV s⁻¹ and 10 mV s⁻¹, whereas electrical impedance spectroscopy measurements were conducted at open circuit potential with an amplitude of 10 mV. The potentials reported versus the RHE are corrected for the electrolyte/cell resistance (~50 Ω) measured using the high-frequency intercept of the real resistance obtained from the Nyquist plot as well as the pH of the electrolyte measured using a pH metre. The electronic resistance between the single-crystal surface and the wire was <5 Ω.

CTR analysis. Surface diffraction measurements were carried out at Beamline 12 ID-D of the Advanced Photon Source, using a similar method described in refs.^{18,22}. The single-crystal surfaces were cleaned by electrochemical cycling between 0.2 V_{RHE} and 1.55 V_{RHE} in 0.1 M HClO₄ solution. Specular and off-specular rods were collected using the reflection geometry for each surface at 1.0 V_{RHE}, 1.3 V_{RHE} and 1.5 V_{RHE}. For a given time, additional rods do not add more information, but increase the signal-to-noise ratio⁵⁸, which can also be obtained by using a longer counting time for the measured rods, as is the case for these measurements. Measurements at high potential were obstructed by evolution of oxygen gas bubbles at the electrode surface. The cell was sealed at the top with an X-ray transparent Kapton foil. To minimize the electrolyte thickness above the sample, air from the cell was sucked out to create a vacuum, using a syringe. Following this, electrolyte was injected through a syringe to form a thin layer above the crystal surface due to capillary forces. The electrolyte used was 0.1 M HClO₄ (70% Veritas double distilled) solution in deionized water (Millipore, >18.2 MΩ cm). The reference electrode used was a saturated Ag/AgCl electrode (Bioanalytical Systems, Inc.) and a platinum counter electrode was used.

The assembled cell was mounted on a Huber five-circle (3S+2D) diffractometer. The initial sample alignment was performed using a laser beam to ensure that the sample surface was at a right angle to the main axis of the diffractometer. Specular rods were recorded using a configuration with the incidence angle equal to the

exit angle. For the off-specular rods, the incidence angle was fixed at either 2° or 4°. An orientation matrix was calculated to relate the motor angles to the Miller indices (*hkl*). The intensities were measured using a pixel area detector (PILATUS 100K model). The measured intensities were extracted by integrating the photon counts of the pixels in the region of interest on the detector and were corrected for background noise, illuminated sample surface area, electrolyte thickness and a Lorentz factor that takes into consideration the experimental geometry.

For each surface, a model was created in GenX version 2.4.7⁵⁹, as discussed in Supplementary Note 3. At each potential, ~200–300 symmetrically independent data points were used for the fitting (Figs. 3 and 4, Supplementary Figs. 5 and 6). The surface model used for the fitting of the (100) data is provided in Supplementary Figs. 7 and 8, and Supplementary Table 5 lists the fitting parameters. Similarly, Supplementary Figs. 9 and 10 show the fitting model used for the (101) surface, and Supplementary Table 10 lists the fitting parameters. For the (100) and (101) surfaces, the adsorbed oxygen atoms were constrained to maintain the bulk bond angle and the validity of this assumption is supported by a good agreement between the CTR bond angle between Ru_{CUS} and O_{1c}, and the corresponding DFT and bulk bond angles shown in Supplementary Fig. 21. Apart from this constraint, all of the other parameters chosen for the CTR analysis are not cross-correlated (that is, allowed to relax independently) to create the simplest model without any a priori assumptions. The figure of merit (FOM) to be minimized is shown in equation (1):

$$\text{FOM}_{\log R1} = \frac{\sum_i |\log(\sqrt{Y_i}) - \log(\sqrt{S_i})|}{\sum_i |\log(\sqrt{Y_i})|} \quad (1)$$

where Y_i is the experimentally measured intensity for point i and S_i is the simulated intensity. All rods were fitted simultaneously and a value <0.10 was obtained for all conditions, signifying a reliable fit (Supplementary Tables 6–8 for the (100) surface and Supplementary Tables 11–13 for the (101) surface). Uncertainties in the bond lengths were obtained by running the simulation ten different times with different initial conditions. The four best simulation results were used to compute the average atomic positions and their s.d., following the method described in ref.⁶⁰. Simulated spectra for various Ru–O_{2c} and Ru–O_{1c} bond lengths are shown in Supplementary Figs. 11–15 for the (100) surface and in Supplementary Figs. 16–18 for the (101) surface. CTR fitting was also carried out on data for the (001) facet (Supplementary Figs. 29–35, Supplementary Tables 19–23, Supplementary Note 9); however, the significant loss of intensity at the anti-Bragg regions suggests a larger surface roughness compared with the (110) and (100) facets, and thus this surface is not included in our analysis.

Surface-enhanced IR spectroscopy. Platinum was first deposited on a silicon plate via an electroless deposition method⁶¹. RuO₂ was sputtered on this film using a ruthenium target at a deposition rate of ~0.7 Å s⁻¹ under Ar:O₂ = 7:5 s.c.c.m., total pressure 3 mTorr, at 450 °C, resulting in a thickness of ~30 nm. X-ray diffraction (Supplementary Fig. 23) and X-ray photoelectron spectroscopy (Supplementary Fig. 24) confirm the presence of rutile RuO₂, which was then pressed against the flat plane of a hemispherical ZnSe prism (radius 22 mm, Pier optics) to increase the signal-to-noise ratio in the lower wavenumber region (that is, lower than 1,400 cm⁻¹). This prism was then mounted in a spectroelectrochemical three-electrode cell. An Ag/AgCl reference electrode and a large surface area platinum wire counter electrode was used. The SEIRA spectra were obtained on a FT-IR Vertex 70 (Bruker) equipped with a mercury cadmium telluride detector (Supplementary Figs. 25 and 26); N₂ was used to fully replace the optical path. The resolution for the measurements was 4 cm⁻¹ and 1,024 scans were averaged for each condition. The SEIRA spectra were recorded using a single-reflection attenuated total reflection accessory (Pike Vee-Max II, Pike Technologies) with a silicon plate/ZnSe prism at an incident angle of 65°. Further experimental details are described elsewhere^{62,63}.

Computational methods. The Vienna ab initio simulation package^{64,65}, using the Perdew–Burke–Ernzerhof functional⁶⁶ and projector augmented-wave projectors^{67,68}, was used for the DFT calculations. A cut-off energy of 500 eV was chosen and a 6 × 6 × 1 Monkhorst–Pack k -point sampling⁶⁹ was used for the super cell. The super cell used for each orientation was a 1 × 2 replication performed along the short axis of the cell. This allowed for symmetry breaking and adsorbate–adsorbate interactions. The Gibbs free energies were calculated by correcting the DFT obtained energies for the zero-point energy and vibrational entropy. The contributions of all atoms beyond the fully reduced surface were considered for the zero-point energy and vibrational entropy contributions. The adsorbed species were referenced to tabulated values of gas-phase hydrogen and water at the gas–liquid interface at 0.035 bar and 300 K respectively⁷⁰. The computational hydrogen electrode described by Nørskov has been used to represent the data on the RHE scale. The gas-phase O₂ reference is calculated using⁷¹ equation (2):

$$0.5 \times G_{\text{O}_2(\text{g})} = G_{\text{H}_2\text{O}(\text{g})} - G_{\text{H}_2(\text{g})} - \Delta G_{\text{exp}} \quad (2)$$

Supplementary Tables 15, 16 and 24 contain the DFT results for the (100), (101) and (001) surfaces, respectively. The atomic coordinates of the optimized models are provided in Supplementary Data 1.

Theoretical Tafel slope analysis. The only potential-dependent term, n_p , used in the estimation of Tafel slope came from potential-dependent coverage of reaction intermediates from DFT (Supplementary Table 17, Supplementary Note 6). At any given potential, the surface coverage of these intermediates must also sum to unity; for example, for the (110) and (100) facets, $\theta_{\text{OOH}} + \theta_{\text{O}} = 1$. The surface coverage of $-\text{O}$ and $-\text{OOH}$ as a function of potential is given by $\theta_{\text{OOH}} = \theta_{\text{O}} e^{-\frac{(\Delta G_{\text{OOH}} - \Delta G_{\text{O}})}{RT}}$, where $\Delta G_{\text{OOH}} - \Delta G_{\text{O}}$ is a function of potential, as can be seen in Fig. 3 for the (100) surface and ref. 18 for the (110) surface. The value of n_i is given by the number of electrons that must be transferred for each active site to be filled with $-\text{OOH}$; thus, for these two surfaces, $n_i = \theta_{\text{O}}$, as each site that is filled with $-\text{O}$ will have to lose one electron to be converted to $-\text{OOH}$. Every site filled with $-\text{OOH}$ can participate in the RDS without further transfer of electrons. For the (101) surface, the RDS is $-\text{O} + \text{H}_2\text{O} - (\text{H}^+ + \text{e}^-) \rightarrow -\text{OO}-\text{H}$. Considering that CTR measurements of (101) at 1.3 V_{RHE} showed that the Ru_{CUS} site is filled with $-\text{OH}$ (full coverage) that became deprotonated at 1.5 V_{RHE}, we lowered the computed binding energy of $-\text{O}$ by 0.15 eV to match the experimental redox transition (Fig. 4). In this case, the $-\text{O}$ species is formed by deprotonation of $-\text{OH}$, $-\text{OH} - (\text{H}^+ + \text{e}^-) \rightarrow -\text{O}$. The surface coverage of $-\text{O}$ and $-\text{OH}$ are related by $\theta_{\text{O}} = \theta_{\text{OH}} e^{-\frac{(\Delta G_{\text{O}} - \Delta G_{\text{OH}})}{RT}}$, where $\Delta G_{\text{O}} - \Delta G_{\text{OH}}$ is potential dependent as seen in Fig. 4. At any given potential, the surface coverage of $-\text{OH}$ and $-\text{O}$ must also follow the relation, $\theta_{\text{OH}} + \theta_{\text{O}} = 1$. In this case, the value of n_i is equal to the surface coverage of $-\text{OH}$ species, as each $-\text{OH}$ species would have to lose one electron to reach the RDS $n_i = \theta_{\text{OH}}$. We note that the surface would become saturated with the intermediates before the RDS at larger overpotentials than the range considered here, resulting in a value of $n_i = 0$ and a Tafel slope of 120 mV per decade.

Data availability

The data supporting the findings of this study are available in the paper and its Supplementary Information. Extra data are available from the corresponding authors on reasonable request.

Received: 22 September 2019; Accepted: 27 March 2020;

Published online: 11 May 2020

References

- Gray, H. B. Powering the planet with solar fuel. *Nat. Chem.* **1**, 7 (2009).
- Andersen, S. Z. et al. A rigorous electrochemical ammonia synthesis protocol with quantitative isotope measurements. *Nature* **570**, 504–508 (2019).
- Liu, C., Colón, B. C., Ziesack, M., Silver, P. A. & Nocera, D. G. Water splitting–biosynthetic system with CO₂ reduction efficiencies exceeding photosynthesis. *Science* **352**, 1210–1213 (2016).
- Zhang, J., Zhao, Z., Xia, Z. & Dai, L. A metal-free bifunctional electrocatalyst for oxygen reduction and oxygen evolution reactions. *Nat. Nanotechnol.* **10**, 444–452 (2015).
- Lee, Y., Suntivich, J., May, K. J., Perry, E. E. & Shao-Horn, Y. Synthesis and activities of rutile IrO₂ and RuO₂ nanoparticles for oxygen evolution in acid and alkaline solutions. *J. Phys. Chem. Lett.* **3**, 399–404 (2012).
- Over, H. Surface chemistry of ruthenium dioxide in heterogeneous catalysis and electrocatalysis: from fundamental to applied research. *Chem. Rev.* **112**, 3356–3426 (2012).
- Chu, Y. S., Lister, T. E., Cullen, W. G., You, H. & Nagy, Z. Commensurate water monolayer at the RuO₂(110)/water interface. *Phys. Rev. Lett.* **86**, 3364–3367 (2001).
- Calle-Vallejo, F. et al. Finding optimal surface sites on heterogeneous catalysts by counting nearest neighbors. *Science* **350**, 185–189 (2015).
- Nørskov, K. J. et al. The nature of the active site in heterogeneous metal catalysis. *Chem. Soc. Rev.* **37**, 2163–2171 (2008).
- Sun, Q., Reuter, K. & Scheffler, M. Effect of a humid environment on the surface structure of RuO₂(110). *Phys. Rev. B* **67**, 205424 (2003).
- Abbott, D. F. et al. Oxygen reduction on nanocrystalline ruthenium—local structure effects. *RSC Adv.* **5**, 1235–1243 (2014).
- Over, H. et al. Atomic-scale structure and catalytic reactivity of the RuO₂(110). *Surf. Sci.* **287**, 1474–1476 (2000).
- Over, H. et al. Visualization of atomic processes on ruthenium dioxide using scanning tunneling microscopy. *ChemPhysChem* **5**, 167–174 (2004).
- Madhavaram, H. et al. Oxidation reactions over RuO₂: a comparative study of the reactivity of the (110) single crystal and polycrystalline surfaces. *J. Catal.* **202**, 296–307 (2001).
- Exner, K. S., Anton, J., Jacob, T. & Over, H. Full kinetics from first principles of the chlorine evolution reaction over a RuO₂(110) model electrode. *Angew. Chem. Int. Ed.* **55**, 7501–7504 (2016).
- Wang, Y., Jacobi, K., Schöne, W.-D. & Ertl, G. Catalytic oxidation of ammonia on RuO₂(110) surfaces: mechanism and selectivity. *J. Phys. Chem. B* **109**, 7883–7893 (2005).
- Wang, Y., Jacobi, K. & Ertl, G. Interaction of NO with the stoichiometric RuO₂(110) surface. *J. Phys. Chem. B* **107**, 13918–13924 (2003).
- Rao, R. R. et al. Towards identifying the active sites on RuO₂(110) in catalyzing oxygen evolution. *Energy Environ. Sci.* **10**, 2626–2637 (2017).
- Roy, C. et al. Trends in activity and dissolution on RuO₂ under oxygen evolution conditions: particles versus well-defined extended surfaces. *ACS Energy Lett.* **3**, 2045–2051 (2018).
- Mu, R. et al. Deprotonated water dimers: the building blocks of segmented water chains on rutile RuO₂(110). *J. Phys. Chem. C* **119**, 23552–23558 (2015).
- Mu, R. et al. Dimerization induced deprotonation of water on RuO₂(110). *J. Phys. Chem. Lett.* **5**, 3445–3450 (2014).
- Rao, R. R. et al. Surface orientation dependent water dissociation on rutile ruthenium dioxide. *J. Phys. Chem. C* **122**, 17802–17811 (2018).
- Stoerzinger, K. A., Qiao, L., Bieganski, M. D. & Shao-Horn, Y. Orientation-dependent oxygen evolution activities of rutile IrO₂ and RuO₂. *J. Phys. Chem. Lett.* **5**, 1636–1641 (2014).
- Hepel, T., Pollak, F. H. & O'Grady, W. E. Effect of crystallographic orientation of single-crystal RuO₂ electrodes on the hydrogen adsorption reactions. *J. Electrochem. Soc.* **131**, 2094–2100 (1984).
- Kuo, D.-Y. et al. Influence of surface adsorption on the oxygen evolution reaction on IrO₂(110). *J. Am. Chem. Soc.* **139**, 3473–3479 (2017).
- Kuo, D.-Y. et al. Measurements of oxygen electroadsorption energies and oxygen evolution reaction on RuO₂(110): a discussion of the sabatier principle and its role in electrocatalysis. *J. Am. Chem. Soc.* **140**, 17597–17605 (2018).
- Stoerzinger, K. A. et al. The role of Ru redox in pH-dependent oxygen evolution on rutile ruthenium dioxide. *Surf. Chem.* **2**, 668–675 (2017).
- Stoerzinger, K. A. et al. Orientation-dependent oxygen evolution on RuO₂ without lattice exchange. *ACS Energy Lett.* **2**, 876–881 (2017).
- Lee, Y.-L., Kleis, J., Rossmeis, J., Shao-Horn, Y. & Morgan, D. Prediction of solid oxide fuel cell cathode activity with first-principles descriptors. *Energy Environ. Sci.* **4**, 3966–3970 (2011).
- Grimaud, A. et al. Activating lattice oxygen redox reactions in metal oxides to catalyse oxygen evolution. *Nat. Chem.* **9**, 457–465 (2017).
- Kim, Y. D., Schwegmann, S., Seitonen, A. P. & Over, H. Epitaxial growth of RuO₂(100) on Ru(1010): surface structure and other properties. *J. Phys. Chem. B* **105**, 2205–2211 (2001).
- Dickens, C. F., Montoya, J. H., Kulkarni, A. R., Bajdich, M. & Nørskov, J. K. An electronic structure descriptor for oxygen reactivity at metal and metal-oxide surfaces. *Surf. Sci.* **681**, 122–129 (2019).
- Dickens, C. F., Kirk, C. & Nørskov, J. K. Insights into the electrochemical oxygen evolution reaction with ab initio calculations and microkinetic modeling: beyond the limiting potential volcano. *J. Phys. Chem. C* **123**, 18960–18977 (2019).
- Vojvodic, A. et al. On the behavior of Bronsted–Evans–Polanyi relations for transition metal oxides. *J. Chem. Phys.* **134**, 244509 (2011).
- Geiger, S. et al. The stability number as a metric for electrocatalyst stability benchmarking. *Nat. Catal.* **1**, 508–515 (2018).
- Ping, Y., Nielsen, R. J. & Goddard, W. A. The reaction mechanism with free energy barriers at constant potentials for the oxygen evolution reaction at the IrO₂ (110) surface. *J. Am. Chem. Soc.* **139**, 149–155 (2017).
- Pedersen, A. F. et al. Operando XAS study of the surface oxidation state on a monolayer IrO₂ on RuO₂ and Ru oxide based nanoparticles for oxygen evolution in acidic media. *J. Phys. Chem. B* **122**, 878–887 (2018).
- Jensen, K. D. et al. Elucidation of the oxygen reduction volcano in alkaline media using a copper–platinum(111) alloy. *Angew. Chem. Int. Ed.* **57**, 2800–2805 (2018).
- Rizo, R., Herrero, E. & Feliu, M. J. Oxygen reduction reaction on stepped platinum surfaces in alkaline media. *Phys. Chem. Chem. Phys.* **15**, 15416–15425 (2013).
- Böckris, J., Reddy, A. & Gamboa-Aldeco, M. *Modern Electrochemistry, 2A: Fundamentals of Electrodes* (Springer, 2000).
- Bockris, J. O. Kinetics of activation controlled consecutive electrochemical reactions: anodic evolution of oxygen. *J. Chem. Phys.* **24**, 817–827 (1956).
- Castelli, P., Trasatti, S., Pollak, F. H. & O'Grady, W. E. Single crystals as model electrocatalysts: oxygen evolution on RuO₂ (110). *J. Electroanal. Chem. Interfacial Electrochem.* **210**, 189–194 (1986).
- Bard, A. J., Faulkner, L. R., Leddy, J. & Zoski, C. G. *Electrochemical Methods: Fundamentals and Applications* Vol. 2 (Wiley, 1980).
- Guiton, T. A. & Pantano, C. G. Infrared reflectance spectroscopy of porous silicas. *Colloids Surf. Physicochem. Eng. Asp.* **74**, 33–46 (1993).
- Huang, Y.-F., Kooyman, P. J. & Koper, M. T. M. Intermediate stages of electrochemical oxidation of single-crystalline platinum revealed by in situ Raman spectroscopy. *Nat. Commun.* **7**, 12440 (2016).
- Frydenlund, R. et al. Benchmarking the stability of oxygen evolution reaction catalysts: the importance of monitoring mass losses. *ChemElectroChem* **1**, 2075–2081 (2014).
- Paoli, E. A. et al. Oxygen evolution on well-characterized mass-selected Ru and RuO₂ nanoparticles. *Chem. Sci.* **6**, 190–196 (2014).
- Wang, T., Jelic, J., Rosenthal, D. & Reuter, K. Exploring pretreatment–morphology relationships: ab initio Wulff construction for RuO₂ nanoparticles under oxidising conditions. *ChemCatChem* **5**, 3398–3403 (2013).

49. Wang, T. & Reuter, K. Structure sensitivity in oxide catalysis: first-principles kinetic Monte Carlo simulations for CO oxidation at RuO₂(111). *J. Chem. Phys.* **143**, 204702 (2015).
50. Dickens, C. F. & Nørskov, J. K. A theoretical investigation into the role of surface defects for oxygen evolution on RuO₂. *J. Phys. Chem. C* **121**, 18516–18524 (2017).
51. Halck, N. B., Petrykin, V., Krttil, P. & Rossmeisl, J. Beyond the volcano limitations in electrocatalysis—oxygen evolution reaction. *Phys. Chem. Chem. Phys.* **16**, 13682–13688 (2014).
52. Chen, D., Fang, Y.-H. & Liu, Z.-P. Searching for active binary rutile oxide catalyst for water splitting from first principles. *Phys. Chem. Chem. Phys.* **14**, 16612–16617 (2012).
53. Lin, Y. et al. Chromium–ruthenium oxide solid solution electrocatalyst for highly efficient oxygen evolution reaction in acidic media. *Nat. Commun.* **10**, 162 (2019).
54. Kadakia, K., Datta, M. K., Jampani, P. H., Park, S. K. & Kumta, P. N. Novel F-doped IrO₂ oxygen evolution electrocatalyst for PEM based water electrolysis. *J. Power Sources* **222**, 313–317 (2013).
55. Duan, L. et al. A molecular ruthenium catalyst with water-oxidation activity comparable to that of photosystem II. *Nat. Chem.* **4**, 418–423 (2012).
56. Lister, T. E. et al. Cathodic activation of RuO₂ single crystal surfaces for hydrogen-evolution reaction. *J. Electroanal. Chem.* **554–555**, 71–76 (2003).
57. Lister, T. E. et al. Electrochemical and X-ray scattering study of well defined RuO₂ single crystal surfaces. *J. Electroanal. Chem.* **524–525**, 201–218 (2002).
58. Gründer, Y. & Lucas, C. A. Surface X-ray diffraction studies of single crystal electrocatalysts. *Nano Energy* **29**, 378–393 (2016).
59. Björck, M. & Andersson, G. GenX: an extensible X-ray reflectivity refinement program utilizing differential evolution. *J. Appl. Crystallogr.* **40**, 1174–1178 (2007).
60. Petach, T. A. et al. Voltage-controlled interfacial layering in an ionic liquid on SrTiO₃. *ACS Nano* **10**, 4565–4569 (2016).
61. Miki, A., Ye, S. & Osawa, M. Surface-enhanced IR absorption on platinum nanoparticles: an application to real-time monitoring of electrocatalytic reactions. *Chem. Commun.* 1500–1501 (2002).
62. Osawa, M., Yoshii, K., Ataka, K. & Yotsuyanagi, T. Real-time monitoring of electrochemical dynamics by submillisecond time-resolved surface-enhanced infrared attenuated-total-reflection spectroscopy. *Langmuir* **10**, 640–642 (1994).
63. Chen, Y. X., Miki, A., Ye, S., Sakai, H. & Osawa, M. Formate, an active intermediate for direct oxidation of methanol on Pt electrode. *J. Am. Chem. Soc.* **125**, 3680–3681 (2003).
64. Kresse, G. & Hafner, J. Ab initio molecular dynamics for liquid metals. *Phys. Rev. B* **47**, 558–561 (1993).
65. Kresse, G. & Furthmüller, J. Efficiency of ab-initio total energy calculations for metals and semiconductors using a plane-wave basis set. *Comput. Mater. Sci.* **6**, 15–50 (1996).
66. Perdew, J. P., Burke, K. & Ernzerhof, M. Generalized gradient approximation made simple. *Phys. Rev. Lett.* **77**, 3865–3868 (1996).
67. Blöchl, P. E. Projector augmented-wave method. *Phys. Rev. B* **50**, 17953–17979 (1994).
68. Kresse, G. & Joubert, D. From ultrasoft pseudopotentials to the projector augmented-wave method. *Phys. Rev. B* **59**, 1758–1775 (1999).
69. Monkhorst, H. J. & Pack, J. D. Special points for Brillouin-zone integrations. *Phys. Rev. B* **13**, 5188–5192 (1976).
70. M. W. Chase et al. *NIST-JANAF Thermochemical Tables v.1.0* (National Institute of Standards and Technology, 1985); <https://janaf.nist.gov/janbanr.html>
71. Nørskov, J. K. et al. Origin of the overpotential for oxygen reduction at a fuel-cell cathode. *J. Phys. Chem. B* **108**, 17886–17892 (2004).

Acknowledgements

This work was supported in part by the Toyota Research Institute through the Accelerated Materials Design and Discovery programme. We thank B. Han for transmission electron microscopy characterization of RuO₂ nanoparticles and J. Corchado-Garcia for help during the CTR data collection. This work was supported in part by the Skoltech-MIT Center for Electrochemical Energy and the Cooperative Agreement between the Masdar Institute, UAE and the Massachusetts Institute of Technology, USA (grant no. 02/MI/MIT/CP/11/07633/GEN/G/00). The work by H.Y. was supported by US Department of Energy (DOE), Basic Energy Sciences (BES), Materials Sciences and Engineering Division, and the work by H.Z. and the use of the Advanced Photon Source were supported by DOE, BES, Scientific User Facility Division (SUFD) under contract no. DE-AC02-06CH11357. The work by A.M. was supported by DOE, BES, SUFD under contract no. DE-AC02-76SF00515. A.F.P. acknowledges the Danish Ministry for Higher Education and Science for an EliteForsk travel grant and the Strategic Research's project NACORR (grant no. 12-133817). This work used the Extreme Science and Engineering Discovery Environment (XSEDE), which is supported by National Science Foundation grant no. ACI-154856283. This research also used resources of the National Energy Research Scientific Computing Center, a DOE Office of Science User Facility supported by the Office of Science of the US DOE under contract no. DE-AC02-05CH11231. T.V. and N.B.H. acknowledge support through V-Sustain: the VILLUM Centre for the Science of Sustainable Fuels and Chemicals (grant no. 9455) from VILLUM FONDEN. I.E.L.S. acknowledges the Peabody Visiting Associate Professorship, awarded by the Department of Mechanical Engineering at Massachusetts Institute of Technology.

Author contributions

Y.S.H. and R.R.R. conceived and designed the experiments. R.R.R. performed the electrochemical measurements. R.R.R., A.F.P., J.H., A.M., H.Y. and H.Z. participated in the surface diffraction measurements. M.J.K., L.G., J.R.L., N.B.H. and T.V. performed the DFT calculations and analysis. Y.K., J.H. and R.R.R. performed the in situ surface-enhanced FT-IR spectroscopy measurements. I.E.L.S. and I.C. participated in the discussion and interpretation of experimental and theoretical data. Y.S.H. and R.R.R. wrote the manuscript. All of the authors discussed the results and commented on the manuscript.

Competing interests

The authors declare no competing interests.

Additional information

Supplementary information is available for this paper at <https://doi.org/10.1038/s41929-020-0457-6>.

Correspondence and requests for materials should be addressed to R.R.R. or Y.S.-H.

Reprints and permissions information is available at www.nature.com/reprints.

Publisher's note Springer Nature remains neutral with regard to jurisdictional claims in published maps and institutional affiliations.

© The Author(s), under exclusive licence to Springer Nature Limited 2020